Space-confined growth of lead-free halide perovskite Cs$_3$Bi$_2$Br$_9$ in MCM-41 molecular sieve as an efficient photocatalyst for CO$_2$ reduction at the gas−solid condition under visible light

Zihao Cui [a], Peng Wang [a,*], Yaqiang Wu [a], Xiaolei Liu [a], Guoqiang Chen [a], Peng Gao [a], Qianqian Zhang [a], Zeyan Wang [a], Zhaoke Zheng [a], Hefeng Cheng [a], Yuanyuan Liu [a], Ying Dai [b], Baibiao Huang [a]

[a] State Key Laboratory of Crystal Materials, Shandong University, Jinan 250100, China
[b] School of Physics, Shandong University, Jinan 250100, China

ARTICLE INFO

ABSTRACT

A facile and effective impregnation method is employed to synthesize the space-confined growth of lead-free halide perovskite Cs$_3$Bi$_2$Br$_9$ in MCM-41 molecular sieve. This MCM-41 @CBB (Cs$_3$Bi$_2$Br$_9$) composite shows an outstanding performance for the photocatalytic reduction of CO$_2$ to CO at the gas−solid condition under visible-light irradiation. The CO production rate of the MCM-41 @ 50 wt% CBB is determined to be 17.24 μmol g^{-1} h^{-1}, which greatly exceeds that of pure CBB (1.89 μmol g^{-1} h^{-1}). The composite is highly stable showing no apparent decrease in the catalytic activity after 8 cycles of repeated experiment. The performance of space-confined growth of CBB nanoparticles in the serial molecular sieve exhibits 2.97–13.4 fold higher than that of pure CBB, respectively, which is superb than CPB (CsPbBr$_3$) and MCM-41 @CPB prepared in the same condition. The results are comparable with those reported for many lead halide perovskites, and are in the top among the lead-free perovskites, especially bismuth halide perovskites.

1. Introduction

The massive consumption of fossil fuels and CO$_2$ emissions exacerbate the well-known energy shortage and global warming issues. Utilizing artificial photosynthesis to convert CO$_2$ into valuable chemical fuels (CO, CH$_4$, CH$_3$OH etc.) is a promising strategy to achieve the goal of zero-emission of CO$_2$, which has aroused great scientific attention as an arrestive technology to further perfect the carbon cycle and achieve carbon neutrality [1–10]. Various semiconductor photocatalysts (such as TiO$_2$, ZnO, BiVO$_4$, etc.) have been explored in the past few decades to promote the CO$_2$ conversion efficiency [11–14]. However, the narrow absorption range of visible light and low photoconversion efficiency still remain huge obstacles [15].

In recent years, the organic-inorganic halide perovskite materials ABX$_3$ (A = CH$_3$NH$_3$$^+$, CH$^-$(NH$_2$)$^{2+}$, Cs$^+$; B = Pb^{2+}; X = Cl$^-$, Br$^-$, I$^-$) have triggered great interest due to their excellent optical absorption, adjustable band gaps, high carriers' mobilities and other prominent photovoltaic properties.[16] They have emerged as attractive candidates in in many fields such as solar cells, [17] light-emitting diodes, [18] photodetectors and so on [19]. Since Park et al. first reported the photocatalytic hydrogen evolution of MAPbI$_3$ in HI solution,[20] the application of perovskite materials employed as photocatalysts has developed remarkably in photocatalytic hydrogen production, [21,22] CO$_2$ reduction, [23] dye degradation, [24] selective oxidation of benzyl alcohol, [25] activation of –CH$_3$ bond and so on.[26] However, the chemical instability of perovskite in polar solvents limits its further application as photocatalyst. In term of photocatalytic CO$_2$ reduction, to address this issue, researchers mainly use perovskite materials in organic solvents such as ethyl acetate and acetonitrile to dissolve CO$_2$ for CO$_2$ reduction.[27] These organic solvents can protect perovskites from exposure to the external environment, ensuring their stability. In addition, gas-solid condition can also guarantee their stability as a more common system in photocatalytic CO$_2$ reduction, but it has been seldom reported at present [28–31]. Moreover, although halide perovskites have great potential in photocatalysis, the further practical application of lead based halide perovskites is hindered by the toxicity of lead [32].

For solar cell applications, people have tried to replace Pb with non-toxic elements such as Sn and Ge, but Sn or Ge based perovskite is not as stable or efficient as lead based perovskite [33,34]. Since the cations Bi^{3+} and Pb^{2+} have similar ionic radii, bismuth seems to be a suitable substitute for lead. Our research group has made some progress in Bi-based perovskite. $Cs_3Bi_{2x}Sb_{2-2x}I_9$ solid solution is demonstrated comparable H_2 evolution performance with $MAPbI_3$ [35].

Perovskite particles generally have large microstructure due to the characteristics of their ionic crystals. The particles size has a distinct effect on their catalytic abilities. In order to overcome this, space-confined growth as a feasible method has been proposed and studied in some fields. For example, Zeng et al. prepared $CsPbBr_3$ film by freezing the precursor solution within the gaps of ordered polystyrene sphere templates and the film exhibited high performance in photodetector [36]. Yu et al. reported the potential applications of hydrochromic $CsPbBr_3$ in anti-counterfeiting by using space-confined $CsPbBr_3$ in mesoporous silica nanospheres [37]. Huang et al. synthesized $MAPbBr_3$ nanocrystals in hollow SiO_2 nanospheres and observed the fluorescence turn-on and wavelength-shift phenomena.[38] Moreover, zeolite molecular sieves are a class of silica aluminate crystal materials with orderly arrangement of pores and regular pore size in structure. These materials have excellent properties such as high specific surface area, nano-sized pore structure, high temperature resistance and adjustable heteroatom content, which are widely used as adsorbents, catalyst carriers and hydrogenation catalysts [39–42]. These merits inspire us that we can use molecular sieve as a carrier to confine the growth of perovskite particles and explore its application in CO_2 reduction in gas-solid condition.

In this work, we confine the growth of lead-free $Cs_3Bi_2Br_9$ nanoparticles in MCM-41 molecular sieve. This MCM-41 @CBB ($Cs_3Bi_2Br_9$) composite shows an outstanding performance for the photocatalytic reduction of CO_2 to CO under visible light irradiation. Space-confined growth of CBB nanoparticles on other molecular sieve such as SBA-3, SBA-15 and MCM-48 are also fabricated, and the activities of them exhibit 2.97–13.4 fold higher than that of pure CBB, respectively. The results are comparable with those reported for many lead halide perovskites, and are in the top among the lead-free perovskites, especially bismuth halide perovskites.

2. Experimental section

2.1. Materials and reagents

Tetraethyl orthosilicate (TEOS), NaOH, Dimethyl sulfoxide (DMSO) and Ethanol was purchased from Sinopharm Chemical Reagent. Hexadecyl trimethyl ammonium Bromide (CTAB), Bismuth bromide ($BiBr_3$, 98%), Lead bromide ($PbBr_2$, 99%), Caesium bromide (CsBr, 99.9%). Hydrobromic acid (HBr, 48 wt% in H_2O) were purchased from Aladdin. All experiment reagents were analytical pure and without further purification.

2.2. Preparation of $Cs_3Bi_2Br_9$ (CBB) powders

$Cs_3Bi_2Br_9$ (CBB) powders were synthesized via a simple coprecipitation method. In a typical procedure, 6 mmol of CsBr was dissolved in 20 mL of hydrobromic acid (48 wt%) and stirred for 30 min. Then 4 mmol of $BiBr_3$ was slowly added into the above solution with continuous stirring for another 30 min under 60 ℃. The resulting solution was cooled down to room temperature to obtain yellow precipitates at the bottom of the beaker. The precipitates were filtered and washed with ethanol for several times and finally dried under vacuum at 80 ℃ for 12 h.

2.3. Preparation of $CsPbBr_3$ (CPB) powders

$CsPbBr_3$ (CPB) sample were obtained through a simple solid state sintering method. Briefly, 10 mmol $PbBr_2$ and 10 mmol CsBr were evenly mixed and ground for about 30 min until the color of mixture powders were changed from white to faint yellow. Then, the ground mixture was transferred to a muffle furnace and heated to 400 ℃ at the rate of 5 ℃ min^{-1} for 2 h. After cooling down to room temperature, the products were ground to get $CsPbBr_3$ powders.

2.4. Preparation of MCM-41

MCM-41 was synthesized via the template synthesis method, which tetraethyl orthosilicate (TEOS) and hexadecyl trimethyl ammonium bromide (CTAB) were used as silicon source and template, respectively. The molar ratio of TEOS, CTAB, NaOH and H_2O was 1:0.12:0.2:100. Typically, 2.428 g of CTAB and 0.447 g of NaOH were dissolved in deionized (DI) water at 40 ℃. Then 11.565 g of TEOS was dripped slowly in the obtained solution with vigorous stirring for 2 h. Afterwards, the homogeneous solution was put into a Teflon–lined stainless steel autoclave and maintained at 120 °C for 24 h. The precipitates were obtained by cooling the solution to room temperature and filtering, after which the precipitates were washed several times with deionized water and ethanol, then dried at 80 °C for 8 h. The MCM-41 powders were finally obtained by calcining at 550 °C for 6 h in muffle furnace. SBA-3, SBA-15 and MCM-48 powders are prepared via similar method.

2.5. Preparation of MCM-41supported CBB

MCM-41 @CBB photocatalyst was prepared via the impregnation method. Specifically, a certain amount of $BiBr_3$ and CsBr were dissolved in 500 μL of Dimethyl sulfoxide (DMSO) with the assistance of ultrasound. Then, the obtained solution was added into MCM-41 powders in a mortar and then pressed for 30 min. The mixture was finally dried at 155 °C for 12 h. A series of MCM-41 @$Cs_3Bi_2Br_9$ samples were obtained through adjusting the weight of $BiBr_3$ and CsBr added to the system. The MCM-41 @$CsPbBr_3$ and other molecular sieve supported $Cs_3Bi_2Br_9$ photocatalysts were obtained using the same method, except that $BiBr_3$ and MCM-41 were replaced by $PbBr_2$ and other molecular sieve, respectively.

2.6. Materials Characterization

The phases and compositions of the as-obtained photocatalysts were performed by XRD measurements on a Rigaku SmartLab 9KW X-ray diffractometer equipped with Cu Kα irradiation. The surface morphologies and detailed structure of the samples were obtained using SEM (Hitachi S-4800) with an energy dispersive spectrometer (EDS). The clear and detailed nanostructure of samples were recorded by TEM and HRTEM (JEOL JEM-2100 F microscope). STEM and STEM mapping were obtained by FEI TalosF200x. X-ray photoelectron spectroscopy (XPS) measurements were carried out using a Thermo Fisher ESCALAB 250XI spectrometer with monochromatized Al Kα excitation to study the surface chemical compositions and states of samples, and C1s (284.8 eV) was used to calibrate the peak positions of various elements. UV–vis diffuse reflectance spectra (DRS) were measured by Shimadzu UV-2600 spectrophotometer equipped with an integrating sphere, with 100% $BaSO_4$ as a reflectance standard to explore the optical absorption. The nitrogen adsorption/desorption isotherms of the samples were characterized on a Kubo-X1000 apparatus to conduct the Brunauer-Emmett-Teller (BET) surface area of the catalysts. CO_2 absorption/desorption measurement (Micromeritics ASAP 2020) was used to study the adsorption capacity of different samples for CO_2. CO_2-TPD and CO-TPD spectra were carried from TP-5080-B. The products were analyzed by GC-7920 gas chromatograph (FID detector, YQ1229 column). In-situ diffuse reflectance infrared Fourier-transform spectroscopy (DRIFTS) were recorded by Nicolet IS50.

2.7. Sample analysis

The catalytic activity of the sample for photocatalytic CO_2 reduction performance was evaluated at atmospheric pressure in a home-made cylindrical reactor (Volume = 45 mL). The temperature of the entire system was kept at 20 °C through a recirculating cooling water system. A 300 W Xe-lamp (CEL-HXF300, Beijing CEAULight, China) equipped with 420 nm cut-off filter was used as a visible light source (λ > 420 nm) and the irradiation density was 350 mW/cm^2 in photocatalytic CO_2 reduction experiments. In a common procedure, 5 mg of sample was spread evenly into a round cap (Diameter = 2.5 cm), then transferred the round cap into the reactor. 500 μL of deionized water was dripped outside the perimeter of cap and then the container was sealed using a quartz cover. Before the reaction, high-purity CO_2 with a flow rate of 10 mL min^{-1} was used to exhaust the air inside the reactor for 30 min. 0.5 mL gas was taken out from the reactor at regular intervals by a syringe and analyzed through an online gas chromatograph (GC-7920 Shimadzu, Japan) equipped with a flame ionized detector (FID). The apparent quantum efficiency (AQE) was measured under the same photocatalytic reaction conditions, with irradiation light through a band-pass filter of 420 nm. The photon flux of the incident light was determined using a PL−MW2000 spectroradiometer (PerfectLight, China). The experimental results indicated CO was the main reduction product for CO_2, thus AQE was defined as the total extracted electron in CO divided by the number of incident photons.

$$AQE = \frac{2 \times N_{CO}}{N} \times 100\%$$

where N_{CO} and N represent the numbers of evolved CO and incident photons, while 2 is the numbers of the required electrons for the conversion of CO_2 to CO.

2.8. Theoretical calculation details

DFT (Density functional theory) calculations were performed using Vienna ab initio simulation package. Projector augmented wave potentials and Perdew-Burke- Ernzerhof (PBE) functional within the generalized gradient approximation (GGA) were considered in the calculation. The (001) crystallographic plane of $Cs_3Bi_2Br_9$ was established for calculation. The cut-off energy was set to be 500 eV, and *k*-point sampling grid was $3 \times 3 \times 1$. The convergence tolerances of energy and force were set 1.0×10^{-4} eV/atom and 1.0×10^{-2} eV/Å. The vacuum space was set to be 15 Å. Moreover, the DFT-D3 method was used to describe the long-range Van der Waals interaction. The adsorption energy (E_{ab}) of CO_2 are defined as:

$E_{ab} = E(\text{sub}+CO_2) – E(\text{sub}) – E(CO_2)$.

Where $E(\text{sub}+ CO_2)$ and $E(\text{sub})$ are the total energy of the system with and without CO_2. $E(CO_2)$ is the total energy of CO_2 molecules. The Gibbs free energy change (ΔG) of the elementary step is calculated by:

$\Delta G = \Delta E + \Delta E_{ZPE} - T\Delta S$.

Where ΔE represents the total energy difference, ΔE_{ZPE} and ΔS are the change in the zero-point energy and the entropy, respectively. T is the temperature set to 298.15 K in this work.

3. Results and discussion

3.1. Synthesis and characterizations of molecular sieves@CBB

The synthesis schematic of MCM-41 supported lead-free halide perovskite CBB with different weight ratio is illustrated in Fig. S1. Firstly, MCM-41 was prepared by one-step hydrothermal method. Then MCM-41 @CBB was further synthesized by using the impregnation method. Meanwhile, for contrast, other different molecular sieves (SBA-3, SBA-15, MCM-48) supported with CBB, pure CBB, lead halide perovskite CPB and MCM-41 supported CPB samples were also synthesized, respectively. The detailed preparation steps of the above mentioned are shown in Experimental Section part.

Fig. 1 and Fig. S2 reveal the powder X-ray diffraction (XRD) profiles of pure MCM-41, CBB and MCM-41 supported CBB with different weight ratios. It can be seen from the small-angle XRD pattern (Fig. 1b) that the prepared samples have the characteristic diffraction peaks of MCM-41. There is no obvious X-ray diffraction peak in the wide-angle of MCM-41 molecular sieve (Fig. 1a), while the characteristic diffraction peaks of CBB begin to appear after loading of CBB into MCM-41 (JCPDS No. 70–493). Moreover, it is found that the diffraction intensities of CBB dramatically increase due to the increase of the loading weight ratios from 10 wt% to 60 wt%. This demonstrates the successful preparation of MCM-41 @CBB composites. Besides, the XRD patterns of pure CPB, MCM-41 supported CPB and other different molecular sieves supported CBB are shown in Fig. S3, Fig. S4 and Fig. S5. The EDS spectrum of the MCM-41 @CBB (Fig. S6) reveals that there are five elements of Si, O, Cs, Bi and Br, and the actual atomic ratio of Cs, Bi, and Br in different photocatalysts are given in Table S1. In order to investigate the elemental composition and the elements chemical states on the surfaces of the obtained samples, X-ray photoelectron spectroscopy (XPS) spectra of MCM-41 @CBB were further carried out and shown in Fig. S7. The C 1 s (284.8 eV) was used to calibrate the peak positions of various elements. Fig. S7a shows the full spectrum of the MCM-41 @CBB sample, where the corresponding peaks of Br 3d Si 2p, Bi 4d, O 1 s and Cs 3d can be clearly seen, which is consistent with EDS results. Fig. S7b is high-resolution XPS spectrum of Cs 3d, the two peaks observed at 724.5 eV and 738.6 eV are assigned to Cs $3d_{5/2}$ and Cs $3d_{3/2}$. The spectrum of Bi 4 f is shown in Fig. S7c, the peaks at 159.6 eV and 164.9 eV coincide with the characteristic peaks of Bi 4 $f_{7/2}$ and Bi 4 $f_{5/2}$, respectively. Moreover, Fig. S7d exhibits the spectrum of Br 3d, where the two peaks located at 68.2 eV and 69.2 eV are ascribed to the Br $3d_{5/2}$ and Br $3d_{3/2}$ peaks.[43] All these results provide a convincing proof for the fact that the samples are successfully prepared.

The scanning electron microscope (SEM) images of pure MCM-41 and MCM-41 supported with different ratios of CBB (10 wt% − 60 wt %) are displayed in Fig. S8a~S8g. The pure MCM-41 particles have smoother surfaces and consist of particles in irregular shape in 1–3 μm in size. The morphologies don't change significantly after loading of CBB, which indicates that the loading process doesn't change the basic structure of the MCM-41 matrix. In addition, very few nanoparticles within 100 nm in average size can be observed on the MCM-41 surface (Fig. S8b~S8g), this is because it is hard to achieve complete uniform dispersion of CBB in MCM-41 using the impregnation method. To further investigate the load state of CBB, transmission electron microscope (TEM) was performed. Fig. 2a, Fig. 2b and Fig. S9 are TEM images of MCM-41. It can be seen that the surface of pure MCM-41 is relatively smooth, which is similar to that observed in its SEM image (Fig. S8a). The regular pore structure of MCM-41 can be observed in Figs. 2a and 2b, and the pore size is about 2 nm. Fig. S10 shows the TEM images of MCM-41 @CBB, and some nanoparticles or nanoclusters with a size of 10–50 nm are tightly deposited on the surface, which are subsequently shown by scanning transmission electron microscopy (STEM) elements mapping to be CBB (Fig. S11). The STEM in high-angle annular dark-field mode (HAADF) images in Fig. 2c, Fig. 2d and Fig. S12 show that the vast majority of halide perovskite is present as small particles around 2–5 nm. Moreover, the regular pore structure can still be remained after loading. STEM EDS and elements mapping in Fig. 2 f~2k and Fig. S12 further prove these small particles are CBB, which are consistent with the results of their powder X-ray diffraction. All these perovskite particles are much smaller in size than pure perovskite particles (about 15 μm in average size. Fig. S8h). The high-resolution TEM (HRTEM) image of Fig. S13 reveals the lattice fringes of CBB in MCM-41 @CBB distinctly. The lattice spacing of 0.31 nm match with the CBB (112) crystallographic plane. It is important to note that, although absolute uniformity is difficult to achieve by impregnation, the SEM and TEM elements mapping measurements for MCM-41 @CBB carried out for the sample
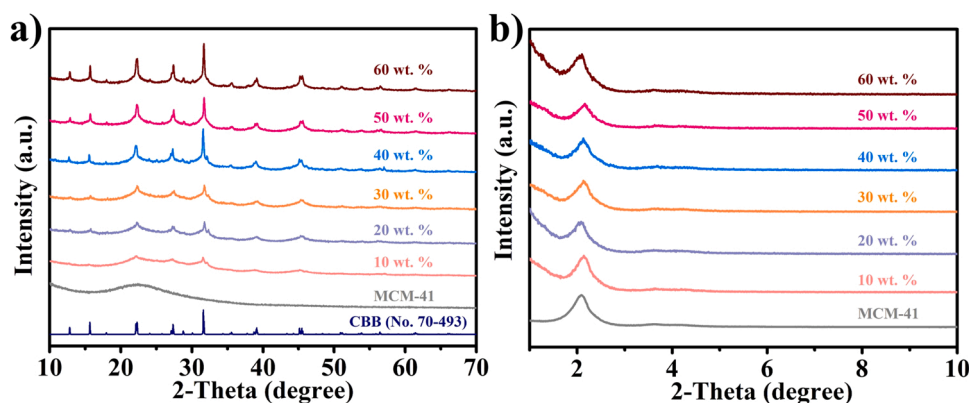
Fig. 1. The large-angle (a) and small-angle (b) XRD patterns of the obtained MCM-41 and MCM-41 @CBB with different weight ratios.
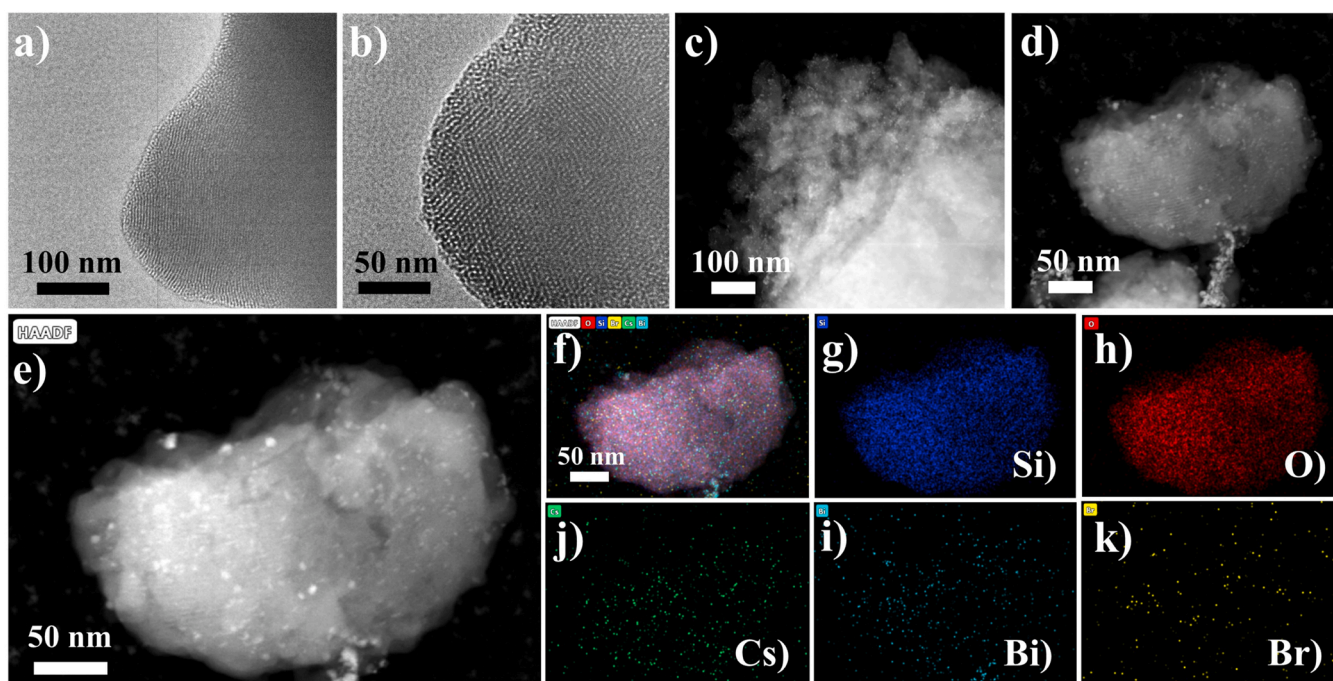

Fig. 2. (a, b) TEM images of MCM-41. (c, d) HAADF-STEM images of MCM-41 @CBB. (e-k) HAADF-STEM elements mapping analysis of MCM-41 @CBB.

area in Fig. S8i, Fig. S14 and Fig. S15 demonstrate that Cs, Bi and Br elements of CBB are evenly distributed in the MCM-41 molecular sieve in the large scale. Besides, the SEM images of other molecular sieves supported CBB are shown in Fig. S16.

Ultraviolet-visible diffuse reflectance spectra (DRS) were carried out to further access the optical properties of as-prepared serial samples. As shown in Fig. 3a, pure MCM-41 doesn't show absorption in the range of 400–800 nm, while the absorption onset of pure CBB is at about 500 nm. The bandgap of pure CBB powder is calculated to be 2.59 eV (Fig. S17), which consists with the previous reports.[43] In addition, visible light absorption appears at about 500 nm when MCM-41 loaded with CBB. With the increase of weight ratio, the light absorption is gradually broadened while the positions of absorption onset don't change significantly. Consistent with this result, the bandgaps of prepared samples are also found to be decreased gradually as the increasing of the loading amount (Fig. S17), which decreases from 2.75 eV to 2.69 eV (10–60 wt %). This can attribute to the quantum confinement effect for smaller nanoparticles [44]. Fig. 3b is the digital photos of as-obtained photocatalysts, the yellow degree of the samples gradually improve with the increase of CBB weight ratio, corresponding with above results. The

UV–vis DRS spectra and optical absorption of pure CPB, MCM-41 @CPB and CBB loaded in other molecular sieve are also recorded in Fig. S18 and Fig. S19, and similar phenomena are also observed.

In addition, the BET surface area and the pore diameter distribution of MCM-41 and MCM-41 @CBB with different loading ratios were characterized to further investigate the space-confined growth of CBB in molecular sieves. Fig. S20a is the N_2 adsorption/desorption isotherms of various samples. It can be seen that pure MCM-41 has a large BET surface area of 945.9482 m^2/g. The BET surface area decreases after loading with CBB. When the loading ratio increases from 10 wt% to 50 wt%, the BET surface area of the sample decreases from 890.8177 m^2/g to 422.0475 m^2/g accordingly (Table S2). This indicates that CBB particles are confined to grow in the pores of MCM-41. However, when the loading ratio reaches 60 wt%, the BET surface area is slightly enhanced compared to that of 50 wt%. This may be because the pores of MCM-41 are almost filled, and the excess CBB particles are loaded on the surface of MCM-41, resulting in an increase in the BET surface area. The N_2 adsorption/desorption isotherms of CBB is shown in Fig. S21, and the BET surface area of CBB is only 0.114 m^2/g (Table S3), which is much smaller than that of MCM-41 @CBB. The pore diameter
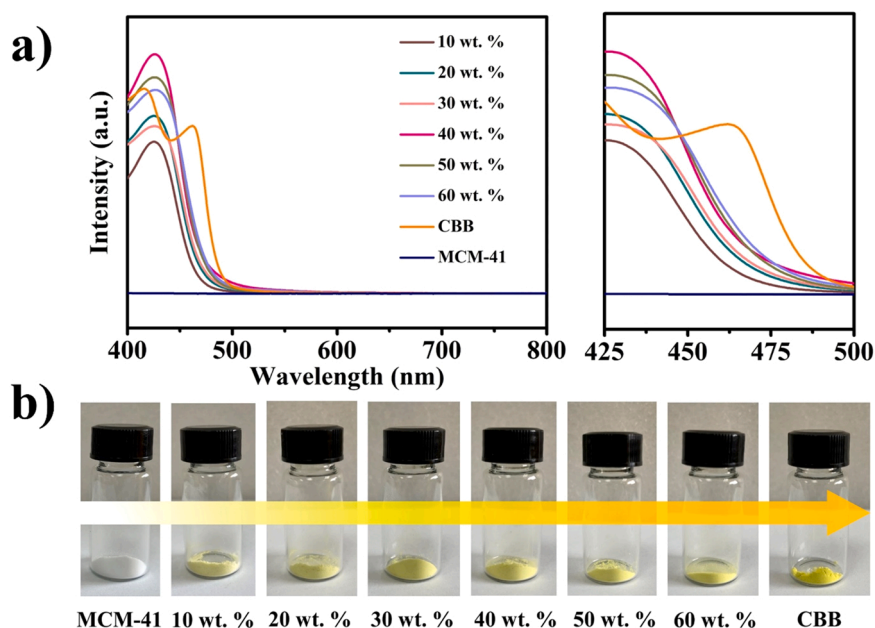
Fig. 3. UV–vis diffuse reflectance spectra (a) and digital photos (b) of MCM-41, CBB and MCM-41 supported CBB with different weight ratios.

distribution of prepared samples is shown in Fig. S20b. Based on the Barret-Joyner-Halenda (BJH) model analysis, the obtained MCM-41 @CBB photocatalysts show a pore size distribution of 2–10 nm calculated from the adsorption branch of the isotherms, which verifies the mesoporous structure of MCM-41. This result also proves that the pore diameter distribution is almost not influenced by the loading process. The average pore diameter of as-prepared samples is about 2 nm, which is consistent with the STEM images observed in Fig. 2. Meanwhile, the BET surface area and the pore diameter distribution of CBB loaded in SBA-3, SBA-15 and MCM-48 are exhibited in the Fig. S22 and Table S4, which also demonstrates similar results.

3.2. Catalytic performance

The photocatalytic performance of as-prepared molecular sieve@CBB photocatalysts was evaluated through the photocatalytic reduction of CO_2 under the irradiation of visible light (λ > 420 nm). The reaction temperature of the reactor was maintained at 20 °C by a circulating cooling system. Fig. 4a presents the activities of MCM-41 @CBB-50 wt% under different conditions. From the experimental results we can find that CO is not produced in the dark, nor is the light irradiation in the absence of photocatalyst. This indicates that the reduction of CO_2 is due to the photocatalytic reaction. To further verify
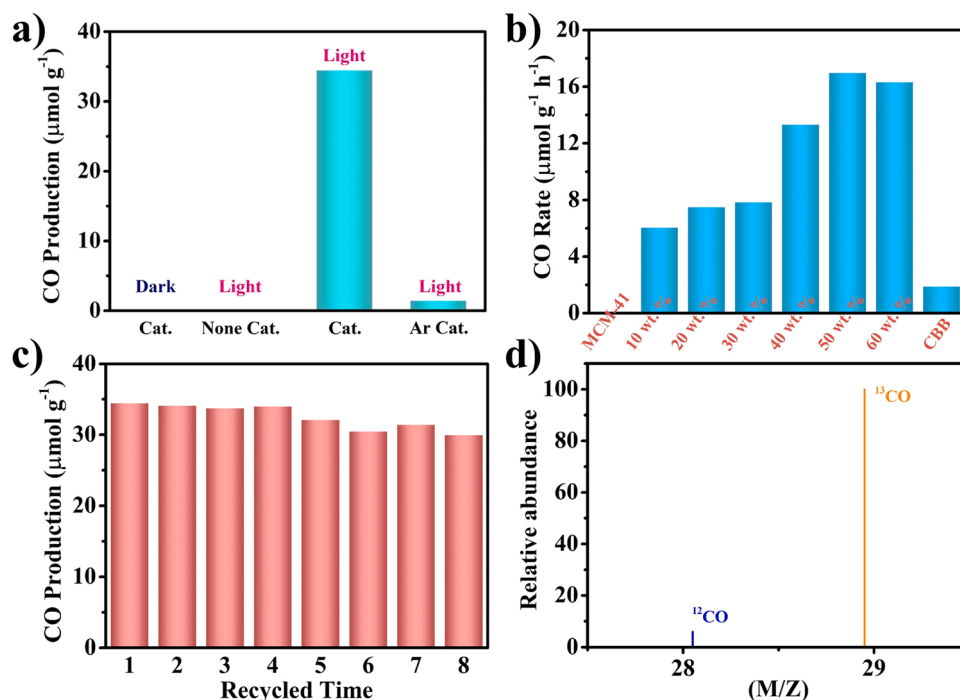

Fig. 4. (a) The photocatalytic performance of MCM-41 @CBB under different conditions. (b) The photocatalytic performance of CBB, MCM-41 and CBB loaded in MCM-41 with different weight ratios. (c) The cycle experiment test of MCM-41 @CBB. (d) (d) GC-MS spectra of the photocatalytic product over MCM-41 @CBB using 13CO2 as carbon source (m/z, mass/charge ratio).

the origin of CO production, a control experiment was examined under the same condition except using Ar to replace CO_2. Only a small amount of CO production is detected under the Ar atmosphere, which can be attributed to the fact that it is difficult to exhaust all CO_2 in the reactor with Ar, resulting in a small amount of CO_2 existing in the reactor. Fig. 4b depicts the photocatalytic CO_2 conversion performance of MCM-41, CBB and MCM-41 @CBB. CBB sample is not efficient for CO production with the rate of about 1.89 μmol g^{-1} h^{-1}. After loading CBB in MCM-41, the composited photocatalysts display superior CO evolution activity, which is due to the fact that the space-confined growth of CBB provides more reaction sites. MCM-41 @CBB 50 wt% exhibits the best performance among them (about 17.24 μmol g^{-1} h^{-1}). In addition, no reduction product is detected for pure MCM-41. Meanwhile, small amount of H_2 can be detected using pure CBB, which is about 0.527 μmol g^{-1} h^{-1} (Fig. S23). However, only CO is detected in the product using series molecular sieve@CBB. This is because the BET surface area of molecular sieve@CBB (400–1000 m^2/g) is much larger than that of CBB (0.114 m^2/g), thus the adsorbed CO_2 is much more than that of CBB. This point is further determined through subsequent CO_2 adsorption measurements and CO_2-TPD spectra. Therefore, the photocatalytic reaction is more inclined to reduce CO_2 to CO rather than H_2 evolution. The CO selectivity of CBB is about 78%, while is nearly 100% in series molecular sieve@CBB photocatalysts. Fig. 4c presents the cyclic stability of MCM-41 @CBB under the same CO_2 photocatalytic reaction conditions. The performance of the photocatalyst remains an acceptable level after eight cycles repeated experiments. The slight decrease of performance may be due to the loss of photocatalyst during the cycle test. Fig. S24 reveals the CO production activity of MCM-41 @CBB under light irradiation through a band-pass filter of 420 nm. The CO production is 0.087 μmol within 2 h irradiation. In this work, the AQE for MCM-41 @CBB at 420 nm is calculated as 1.8×10^{-3}%. Moreover, $^{13}CO_2$ isotope trace experiment was also investigated to further probe the origination of CO. Fig. 4d shows the corresponding GC-MS spectra. The major mass spectrum signals with m/z value of 29 (^{13}CO) can be observed, revealing that CO originates from photocatalytic CO_2 reduction. Besides, we also conducted control experiments on lead halide perovskite CPB and MCM-41 @CPB. As shown in Fig. S25, there is almost no CO detected under the same condition using CPB and MCM-41 @CPB, which is a strange phenomenon and needs to be further explored. Meanwhile, We further investigated the photocatalytic CO_2 reduction performance of CBB supported by other molecular sieves. The results are shown in Fig. S26. The photocatalytic CO_2 reduction activities of CBB loaded in SBA-3, SBA-15 and MCM-48 molecular sieves are better than that of primal CBB. The CO evolution rates of SBA-3 @CBB, SBA-15 @CBB and MCM-48 @CBB are 25.4 μmol g^{-1} h^{-1}, 23.7 μmol g^{-1} h^{-1} and 5.62 μmol g^{-1} h^{-1}, respectively, which exhibits 2.97–13.4 fold higher than that of pure CBB. The results demonstrate that the space-confined growth of CBB in molecular sieve is a general approach to improve the photocatalytic CO_2 reduction performance. The results are comparable with many reported lead halide perovskites, and are excellent among the lead-free perovskites, especially bismuth halide perovskites (Table S5 and S6).

3.3. Proposed mechanism

To further investigate the probable mechanism for photocatalytic CO_2 reduction by MCM-41 @CBB, CO_2 adsorption measurements of CBB and MCM-41 @CBB were carried out. Fig. S27 presents the CO_2 adsorption/desorption isotherms. MCM-41 @CBB composites show better CO_2 adsorption capacity than that of pure CBB. In general, better adsorption capacity can promote the reaction, and the adsorbed CO_2 can be reduced more effectively by photocatalyst. Thus, it might be a reason why the photocatalytic CO_2 reduction performance is enhanced. To further investigate the adsorption behavior of CO_2 and CO over the prepared samples, the temperature-programmed desorption of CO_2 (CO_2-TPD) and CO (CO-TPD) were carried out. CO_2-TPD (CO-TPD) is

considered as a sensitive technology which can provide detailed information on the interaction between adsorbed CO_2 (CO) molecules and photocatalyst surfaces [45–47]. CO_2-TPD spectra of CBB and MCM-41 @CBB are compared in Fig. S28a. The active sites for photocatalytic CO_2 reduction can be evaluated through the total area under the curve of all desorption peaks. The peak area of MCM-41 @CBB is larger than CBB, which further proves that the adsorption capacity of CO_2 can be significantly improved in MCM-41 @CBB [48,49]. This is beneficial to the photocatalytic CO_2 reduction process. Simultaneously, the desorption temperature of MCM-41 @CBB moves towards high temperature, indicating that the binding of CO_2 molecules with MCM-41 @CBB photocatalyst is stronger [50,51]. The activation energy barrier for photocatalytic CO_2 reduction is subsequently decreased owing to such strong interaction. Similarly, the CO-TPD spectra in Fig. S28b show the peak area of CBB is lower than that of MCM-41 @CBB, indicating the adsorption capacity of CO is also be improved. This can be ascribed to the large specific surface area of MCM-41 @CBB. Meanwhile, the CO desorption temperature of MCM-41 @CBB also shifts towards high temperature. These results also show that CO adsorption is not the main factor of photocatalytic efficiency in this work. Furthermore, in-situ diffuse reflectance infrared Fourier-transform spectroscopy (DRIFTS) measurements were performed on MCM-41 @CBB under the reaction operando conditions to deeply elucidate the catalytic pathway for photocatalytic CO_2 reduction progress. The CO_2 bubbling in the water was passed into the in-situ pool for 20 min, and then the in-situ pool was closed and illuminated. Fig. S29 presents the transient evolution DRIFTS spectra. Two peaks at 2311 cm^{-1} and 2315 cm^{-1} ascribed to the asymmetric stretching of CO_2 in the environment [52,53]. These two peaks don't appear when there is no CO_2 injected, and the intensity of these two peaks increases gradually with the CO_2 entered. There is no obvious change in the peak intensity after 15 min and 20 min, which indicates that the CO_2 in the in-situ pool is saturated. As the beginning of irradiation, the intensity of these two peaks decreased slightly, and the intensity is further decreased with the extension of the irradiation time. This result reveals that part of the CO_2 has undergone photocatalytic reaction, and also shows that the reduction products come from CO_2. Fig. 5a presents the detail transient evolution of the surface species during CO_2 adsorption progress. The bands at 1621 cm^{-1} and 1648 cm^{-1} are assigned to absorbed CO_2 species including bidentate carbonate (b-CO_3^{2-}) and bicarbonate (HCO_3^-) [54–56]. The intensity of these two bands increase with the development of CO_2 injection time. Upon exposure of the closed in-situ pool to light irradiation, as shown in Fig. 5b, the pristine bands of bidentate carbonate and bicarbonate vanish, while the new obvious IR feature appears at 1310 cm^{-1}. This can be attributed to the symmetric OCO stretching vibration of monodentate carbonate (m-CO_3^{2-}) [13,57,58]. The intensity of this band is also increased with the increase of irradiation time, which indicates that the monodentate carbonate can be regarded as the key intermediate during reduction of CO_2 to CO. Moreover, the antisymmetric OCO stretching vibration of *COOH group appears at 1558 cm^{-1} and increases slightly with the increase of irradiation time, suggesting that small amount of formate is formed during the CO_2 reduction progress [57,59]. Therefore, part of the CO in the product may come from the dissociation of carboxyl compounds.

Based on the above results, the following possible hypothesis is proposed rationally to access the CO_2 photocalalytic reduction mechanism. As shown in Fig. 6a, the conduction band minimum (CBM) and valence band maximum (VBM) energy levels of synthesized MCM-41 @CBB composite are conducted from the UPS measurement (Fig. S30), which are 2.3 eV and − 0.4 eV, respectively. According to the reference, Bi p orbitals contribute the most to CBM, while Br 4p orbitals assigned to VBM.[43,60] During the CO_2 adsorption process under darkness, the MCM-41 @CBB photocatalytic has high CO_2 adsorption performance, which CO_2 is adsorbed on the surface of the catalyst to form bicarbonate and bidentate carbonate until the adsorption reaches saturation. When light is irradiated, photo-generated holes and electrons
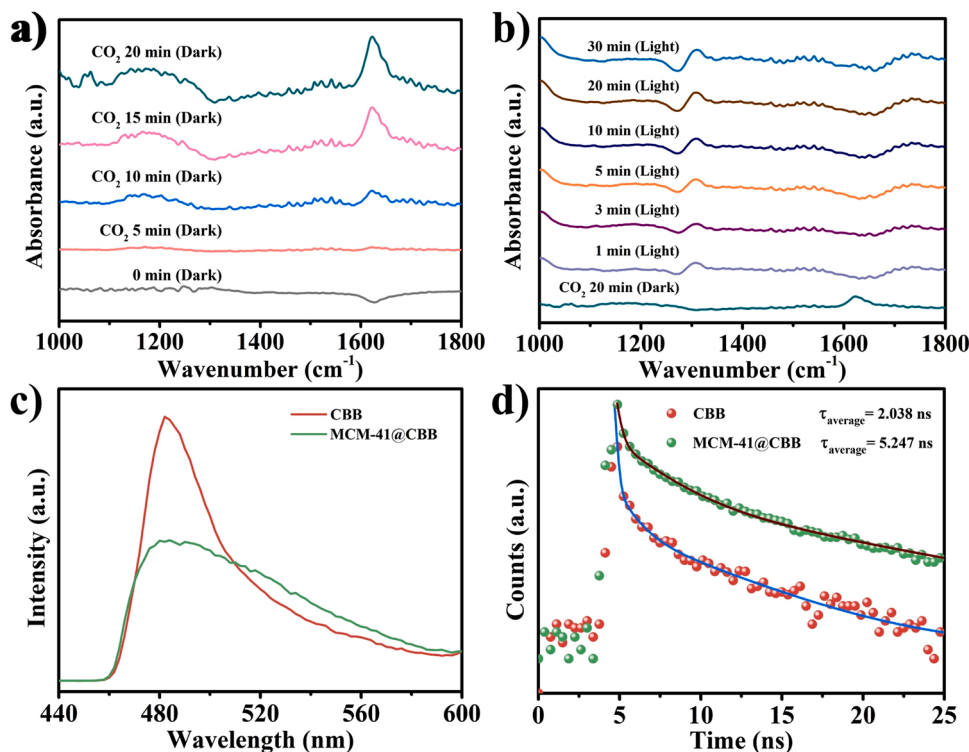
Fig. 5. In-situ DRIFTS spectra of MCM-41 @CBB under (a) dark and (b) light irradiation. (c) Steady-state PL spectra and (d) PL decay spectra of CBB and MCM-41 @CBB collected at the indicated emission wavelengths with 409 nm laser excitation light at room temperature.

appear on the VBM and CBM, respectively. Then, the separation of electron-hole pairs is enhanced in the MCM-41 @CBB photocatalyst due to the existence of more reaction sites, which is further proved through steady-state photoluminescence (PL) spectra and time-resolved photoluminescence (TRPL) spectra. As shown in Fig. 5c, the emission intensity of CBB is higher than that of MCM-41 @CBB, which illustrates electron-hole pair separation is enhanced in MCM-41 @CBB sample. Moreover, Fig. 5d shows the time-resolved photoluminescence (TRPL) spectra CBB and MCM-41 @CBB. The PL decay traces are fitted via a three-exponential function, and the interrelated average decay times are listed in Table S7. The CBB exhibits a carrier lifetime of 2.038 ns, which is less than that of MCM-41 @CBB (5.274 ns), revealing good agreement with the PL spectra results. Thus, the space-confined growth of CBB in MCM-41 molecular sieve can promote the carrier's lifetime significantly, which is favorable for the electron-hole pair separation and subsequent transfer.

Furthermore, DFT calculations was performed to explain the mechanism of photocatalytic CO_2 reduction. Fig. 6b is the interaction model of CBB in MCM-41 molecular sieve and CO_2 molecules during the photocatalytic CO_2 reduction process. The adsorbed CO_2 on the molecular sieve is further in contact with CBB in the molecular sieve. After optimization, the adsorption site is determined as Cs or Br atom in CBB. Specifically, the C atom of CO_2 interacts with the Cs atom of CBB, or the C and O atoms of CO_2 interact with the Cs and Br atom of CBB, respectively. The adsorption energies of these two types are − 0.1613 eV and − 0.2803 eV, respectively. Negative adsorption energy values indicate that the adsorption of CO_2 molecules on CBB is favorable. Subsequently, the adsorbed CO_2 will react with the separated photo-generated electrons to produce relevant intermediates, finally converted to CO. Moreover, the corresponding Gibbs free energies (ΔG) for each reaction steps are calculated. As depicted in Fig. 6c and 6d, the formation of *COOH from *CO_2 is considered as the rate-determining step under the two adsorption conditions. Combined with CO_2-TPD and DFT calculation results, the molecular sieve not only promoted the adsorption of CO_2 molecules, but also reduced the energy barrier of CO_2

activation. Thus the transformation of CO_2 molecules is promoted.

4. Conclusion

In summary, we achieve the lead-free halide perovskite CBB space-confined growth in MCM-41 molecular sieve using a facile and efficient impregnation method, and then evaluate their photocatalytic activities for the CO_2 reduction in gas-solid condition. The samples have superb performance in photocatalytic CO_2 reduction. The performance of space-confined growth of CBB nanoparticles in the serial molecular sieve exhibits 2.97–13.4 fold higher than that of pure CBB, respectively. The composite is highly stable showing no apparent decrease in the catalytic activity after 5 cycles of repeated experiment. The monodentate carbonate can be regarded as the key intermediate during the CO_2 reduction progress. Our study not only provides an approach to confine the growth of perovskite nanoparticles, but also supplies a new idea in investigating their application in catalysis.

CRediT authorship contribution statement

Zihao Cui: Formal analysis, Methodology, Data curation, Resources, Investigation, Writing – original draft, Writing – review & editing. **Peng Wang:** Conceptualization, Supervision, Writing – review & editing, Project administration, Funding acquisition. **Yaqiang Wu:** Methodology, Validation. **Xiaolei Liu:** Methodology, Validation. **Guoqiang Chen:** Methodology, Investigation. **Peng Gao:** Investigation. **Qianqian Zhang:** Validation. **Zeyan Wang:** Methodology. **Zhaoke Zheng:** Validation. **Hefeng Cheng:** Investigation. **Yuanyuan Liu:** Investigation, Validation. **Ying Dai:** Software, Validation. **Baibiao Huang:** Conceptualization, Supervision, Project administration, Funding acquisition.

Declaration of Competing Interest

The authors declare that they have no known competing financial interests or personal relationships that could have appeared to influence
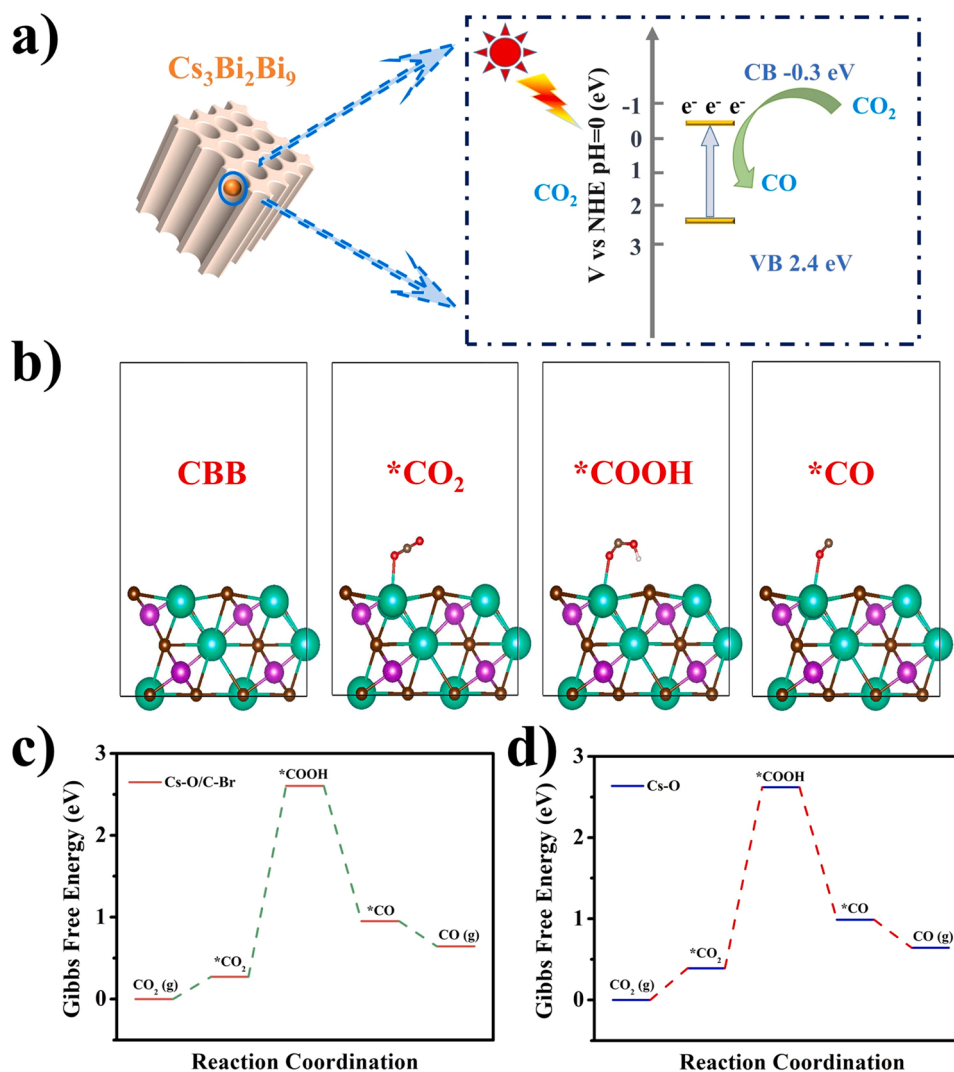
Fig. 6. (a) The possible mechanism of CO_2 reduction for the MCM-41 @CBB. (b) The interaction model of CBB and CO_2 molecules during the photocatalytic CO_2 reduction process. (c, d) Gibbs free energy diagrams of photocatalytic CO_2 reduction to CO at different adsorption sites.

the work reported in this paper.

Appendix A. Supporting information

Supplementary data associated with this article can be found in the online version at doi:10.1016/j.apcatb.2022.121375.

References

[1] X. Li, P. Wang, Y.-Q. Wu, Z.-H. Liu, Q.-Q. Zhang, T.-T. Zhang, Z.-Y. Wang, Y.-Y. Liu, Z.-K. Zheng, B.-B. Huang, ZnGeP$_2$: A near-infrared-activated photocatalyst for hydrogen production, Front. Phys. 15 (2020) 23604.

[2] Y. Wu, Q. Wu, Q. Zhang, Z. Lou, K. Liu, Y. Ma, Z. Wang, Z. Zheng, H. Cheng, Y. Liu, Y. Dai, B. Huang, P. Wang, An organometal halide perovskite supported Pt single-atom photocatalyst for H$_2$ evolution, Energy Environ. Sci. (2022), https://doi.org/10.1039/d1ee03679c.

[3] X. Liu, P. Wang, X. Liang, Q. Zhang, Z. Wang, Y. Liu, Z. Zheng, Y. Dai, B. Huang, Research progress and surface/interfacial regulation methods for electrophotocatalytic hydrogen production from water splitting, Mater. Toady Energy 18 (2020), 100524.

[4] X. Liu, P. Wang, H. Zhai, Q. Zhang, B. Huang, Z. Wang, Y. Liu, Y. Dai, X. Qin, X. Zhang, Synthesis of synergetic phosphorus and cyano groups (C⚌N) modified g-C$_3$N$_4$ for enhanced photocatalytic H$_2$ production and CO$_2$ reduction under visible light irradiation, Appl. Catal. B: Environ. 232 (2018) 521–530.

[5] J. Fu, K. Jiang, X. Qiu, J. Yu, M. Liu, Product selectivity of photocatalytic CO$_2$ reduction reactions, Mater. Today 32 (2020) 222–243.

[6] X. Li, J. Yu, M. Jaroniec, X. Chen, Cocatalysts for selective photoreduction of CO$_2$ into solar fuels, Chem. Rev. 119 (2019) 3962–4179.

[7] R. Cheng, C.C. Chung, S. Wang, B. Cao, M. Zhang, C. Chen, Z. Wang, M. Chen, S. Shen, S.P. Feng, Three-dimensional self-attaching perovskite quantum dots/polymer platform for efficient solar-driven CO$_2$ reduction, Mater. Today Phys. 17 (2021), 100358.

[8] Y. Gao, Q. Wu, X. Liang, Z. Wang, Z. Zheng, P. Wang, Y. Liu, Y. Dai, M.H. Whangbo, B. Huang, Cu$_2$O nanoparticles with both {100} and {111} facets for enhancing the selectivity and activity of CO$_2$ electroreduction to ethylene, Adv. Sci. 7 (2020) 1902820.

[9] L. Wang, L. Wang, Y. Du, X. Xu, S.X. Dou, Progress and perspectives of bismuth oxyhalides in catalytic applications, Mater. Today Phys. 16 (2021) 100294.

[10] Z. Wang, J. Fan, B. Cheng, J. Yu, J. Xu, Nickel-based cocatalysts for photocatalysis: hydrogen evolution, overall water splitting and CO_2 reduction, Mater. Today Phys. 15 (2020), 100279.

[11] C. Kim, K.M. Cho, A. Al-Saggaf, I. Gereige, H.-T. Jung, Z-scheme photocatalytic CO_2 conversion on three-dimensional $BiVO_4$/carbon-coated Cu_2O Nanowire Arrays under Visible Light, ACS, Catalysis 8 (2018) 4170–4177.

[12] J. Yu, J. Low, W. Xiao, P. Zhou, M. Jaroniec, Enhanced photocatalytic CO_2 reduction activity of anatase TiO_2 by coexposed {001} and {101} facets, J. Am. Chem. Soc. 136 (2014) 8839–8842.

[13] G. Yin, X. Huang, T. Chen, W. Zhao, Q. Bi, J. Xu, Y. Han, F. Huang, Hydrogenated blue titania for efficient solar to chemical conversions: preparation, characterization, and reaction mechanism of CO_2 reduction, ACS Catal. 8 (2018) 1009–1017.

[14] Y. He, Y. Wang, L. Zhang, B. Teng, M. Fan, High-efficiency conversion of CO_2 to fuel over ZnO/g-C_3N_4 photocatalyst, Appl.Catalysis B: Environ. 168–169 (2015) 1–8.

[15] J.K. Stolarczyk, S. Bhattacharyya, L. Polavarapu, J. Feldmann, Challenges and prospects in solar water splitting and CO_2 reduction with inorganic and hybrid nanostructures, ACS Catalysis 8 (2018) 3602–3635.

[16] W.W. Chen, Y. Yue, Y. Liu, J. Zhang, W. Yang, X. Chen, H. Bi, E. Ashraful, I. Gratzel, M. Han, L, Efficient and stable large-area perovskite solar cells with inorganic charge extraction layers, Science 350 (2015) 9441948.

[17] H. Min, M. Kim, S.U. Lee, H. Kim, G. Kim, K. Choi, J.H. Lee, S.I. Seok, Efficient, stable solar cells by using inherent bandgap of a-phase formamidinium lead iodide, Science 366 (2019) 749–753.

[18] Z.K. Tan, R.S. Moghaddam, M.L. Lai, P. Docampo, R. Higler, F. Deschler, M. Price, A. Sadhanala, L.M. Pazos, D. Credgington, F. Hanusch, T. Bein, H.J. Snaith, R. H. Friend, Bright light-emitting diodes based on organometal halide perovskite, Nat. Nanotechnol. 9 (2014) 687–692.

[19] M.I. Saidaminov, V. Adinolfi, R. Comin, A.L. Abdelhady, W. Peng, I. Dursun, M. Yuan, S. Hoogland, E.H. Sargent, O.M. Bakr, Planar-integrated single-crystalline perovskite photodetectors, Nat. Commun. 6 (2015) 8724.

[20] S. Park, W.J. Chang, C.W. Lee, S. Park, H.-Y. Ahn, K.T. Nam, Photocatalytic hydrogen generation from hydriodic acid using methylammonium lead iodide in dynamic equilibrium with aqueous solution, Nat. Energy 2 (2016) 16185.

[21] Y. Wu, P. Wang, X. Zhu, Q. Zhang, Z. Wang, Y. Liu, G. Zou, Y. Dai, M.H. Whangbo, B. Huang, Composite of $CH_3NH_3PbI_3$ with reduced graphene oxide as a highly efficient and stable visible-light photocatalyst for hydrogen evolution in aqueous HI solution, Adv. Mater. 30 (2018) 1704342.

[22] Y. Wu, P. Wang, Z. Guan, J. Liu, Z. Wang, Z. Zheng, S. Jin, Y. Dai, M.-H. Whangbo, B. Huang, Enhancing the photocatalytic hydrogen evolution activity of mixed-halide perovskite $CH_3NH_3PbBr_{3-x}I_x$ achieved by bandgap funneling of charge carriers, ACS Catalysis 8 (2018) 10349–10357.

[23] W.T. Man Ou, Shengming Yin, Weinan Xing, Shuyang Wu, Haojing Wang, Shipeng Wan, Qin Zhong, Rong Xu, Amino-assisted anchoring of $CsPbBr_3$ perovskite quantum dots on porous g-C_3N_4 for enhanced photocatalytic CO_2 reduction, Angew. Chem. Int. Ed. 130 (2018) 13758–13762.

[24] Z. Zhang, Y. Liang, H. Huang, X. Liu, Q. Li, L. Chen, D. Xu, Stable and highly efficient photocatalysis with lead-free double-perovskite of $Cs_2AgBiBr_6$, Angew. Chem. 58 (2019) 7263–7267.

[25] H. Huang, H. Yuan, K.P.F. Janssen, G. Solís-Fernández, Y. Wang, C.Y.X. Tan, D. Jonckheere, E. Debroye, J. Long, J. Hendrix, J. Hofkens, J.A. Steele, M.B. J. Roeffaers, Efficient and selective photocatalytic oxidation of benzylic alcohols with hybrid organic–inorganic perovskite materials, ACS Energy Lett. 3 (2018) 755–759.

[26] H. Huang, H. Yuan, J. Zhao, G. Solís-Fernández, C. Zhou, J.W. Seo, J. Hendrix, E. Debroye, J.A. Steele, J. Hofkens, J. Long, M.B.J. Roeffaers, C(sp³)–H bond activation by perovskite solar photocatalyst cell, ACS Energy Lett. 4 (2018) 203–208.

[27] Y.F. Xu, M.Z. Yang, B.X. Chen, X.D. Wang, H.Y. Chen, D.B. Kuang, C.Y. Su, A. $CsPbBr3$, Perovskite quantum dot/graphene oxide composite for photocatalytic CO_2 reduction, J. Am. Chem. Soc. 139 (2017) 5660–5663.

[28] Y. Jiang, H.Y. Chen, J.Y. Li, J.F. Liao, H.H. Zhang, X.D. Wang, D.B. Kuang, Z-scheme 2D/2D heterojunction of $CsPbBr_3$/Bi_2WO_6 for improved photocatalytic CO_2 reduction, Adv. Funct. Mater. 30 (2020) 2004293.

[29] H. Huang, B. Pradhan, J. Hofkens, M.B.J. Roeffaers, J.A. Steele, Solar-driven metal halide perovskite photocatalysis: design, stability, and performance, ACS Energy Lett. 5 (2020) 1107–1123.

[30] Y. Jiang, J.-F. Liao, H.-Y. Chen, H.-H. Zhang, J.-Y. Li, X.-D. Wang, D.-B. Kuang, All-solid-state Z-scheme α-Fe_2O_3/Amine-RGO/$CsPbBr_3$ hybrids for visible-light-driven photocatalytic CO_2 reduction, Chem 6 (2020) 766–780.

[31] Y. Wang, H. Huang, Z. Zhang, C. Wang, Y. Yang, Q. Li, D. Xu, Lead-free perovskite $Cs_2AgBiBr_6$@g-C_3N_4 Z-scheme system for improving CH_4 production in photocatalytic CO_2 reduction, Appl. Catal. B: Environ. 282 (2021), 119570.

[32] Q. Fan, G.V. Biesold-McGee, J. Ma, Q. Xu, S. Pan, J. Peng, Z. Lin, Lead-free halide perovskite nanocrystals: crystal structures, synthesis, stabilities, and optical properties, Angew. Chem. 59 (2020) 1030–1046.

[33] N.K. Noel, S.D. Stranks, A. Abate, C. Wehrenfennig, S. Guarnera, A.-A. Haghighirad, A. Sadhanala, G.E. Eperon, S.K. Pathak, M.B. Johnston, A. Petrozza, L.M. Herz, H.J. Snaith, Lead-free organic–inorganic tin halide perovskites for photovoltaic applications, Energy Environ. Sci. 7 (2014) 3061–3068.

[34] T. Krishnamoorthy, H. Ding, C. Yan, W.L. Leong, T. Baikie, Z. Zhang, M. Sherburne, S. Li, M. Asta, N. Mathews, S.G. Mhaisalkar, Lead-free germanium iodide

[35] G. Chen, P. Wang, Y. Wu, Q. Zhang, Q. Wu, Z. Wang, Z. Zheng, Y. Liu, Y. Dai, B. Huang, Lead-free halide perovskite $Cs_3Bi_{2x}Sb_{2-2x}I_9$ (x approximately 0.3) possessing the photocatalytic activity for hydrogen evolution comparable to that of (CH_3 NH_3)PbI_3, Adv. Mater. 32 (2020), 2001344.

[36] J. Zeng, X. Li, Y. Wu, D. Yang, Z. Sun, Z. Song, H. Wang, H. Zeng, Space-confined growth of $CsPbBr_3$ film achieving photodetectors with high performance in all figures of merit, Adv. Funct. Mater. 28 (2018) 1804394.

[37] L.W. Xiaoya Yu, Di Yang, Muhan Cao, Xing Fan, Haiping Lin, Qixuan Zhong, Yong Xu, Qiao Zhang, Hydrochromic CsPbBr3 Nanocrystals Anti-Count., Angew. Chem. Int. Ed. 59 (2020) 14527–14532.

[38] Y. Huang, S. Wang, Y. Zhu, F. Li, J. Jin, J. Dong, F. Lin, Y. Wang, X. Chen, Dual-mode of fluorescence turn-on and wavelength-shift for methylamine gas sensing based on space-confined growth of methylammonium lead tribromide perovskite nanocrystals, Anal. Chem. 92 (2020) 5661–5665.

[39] J.S. Hwajun Lee1, Kyounghwan Lee, Hyun June Choi, Alvaro Mayoral, Na Young Kang, Suk Bong Hong, Synthesis of thermally stable SBT and SBS/SBT intergrowth zeolites, Science 373 (2021) 104–107.

[40] P.H.H. Niklas Pfriem, Sebastian Eckstein, Sungmin Kim, Qiang Liu, Hui Shi, Lara Milakovic, Yuanshuai Liu, Gary L. Haller, Eszter Baráth, Yue Liu, Johannes A. Lercher, Role of the ionic environment in enhancing the activity of reacting molecules in zeolite pores, Science 372 (2021) 952–957.

[41] X.Y. Hang Zhou1, Yu Hui, Liang Wang, Wei Chen, Yucai Qin, Ming Wang, Jiabi Ma, Xuefeng Chu, Yeqing Wang, Xin Hong, Zifeng Chen, Xiangju Meng, Hai Wang, Qiuyan Zhu, Lijuan Song, Anmin Zheng, Feng-Shou Xiao, Isolated boron in zeolite for oxidative dehydrogenation of propane, Science 372 (2021) 76–80.

[42] L.W. Zhu Jin1, Erik Zuidema, Kartick Mondal, Ming Zhang, Jian Zhang, Chengtao Wang, Xiangju Meng, Hengquan Yang, Carl Mesters, Feng-Shou Xiao, Hydrophobic zeolite modification for in situ peroxide formation in methane oxidation to methanol, Science 367 (2020) 193–197.

[43] M. Shi, G. Li, W. Tian, S. Jin, X. Tao, Y. Jiang, E.A. Pidko, R. Li, C. Li, Understanding the effect of crystalline structural transformation for lead-free inorganic halide perovskites, Adv. Mater. 32 (2020), e2002137.

[44] S.N. Andrew, M. Smith, Semiconductor nanocrystals: structure, properties, and band gap engineering, ACC Chem. Res. 43 (2010) 190–200.

[45] K. Teramura, S.-i Okuoka, H. Tsuneoka, T. Shishido, T. Tanaka, Photo Reduct. CO2 Using H.2 reductant ATaO3 Photocatal. (A=Li, Na, K.), Appl. Catal. B: Environ. 96 (2010) 565–568.

[46] H. Li, B. Zhu, S. Cao, J. Yu, Controlling defects in crystalline carbon nitride to optimize photocatalytic CO_2 reduction, Chem. Commun. 56 (2020) 5641–5644.

[47] J. Guo, K. Wang, X. Wang, Photocatalytic reduction of CO_2 with H_2O vapor under visible light over Ce doped $ZnFe_2O_4$, Catal. Sci. Technol. 7 (2017) 6013–6025.

[48] S. Zhu, S. Liang, J. Bi, M. Liu, L. Zhou, L. Wu, X. Wang, Photocatalytic reduction of CO_2 with H_2O to CH_4 over ultrathin $SnNb_2O_6$ 2D nanosheets under visible light irradiation, Green. Chem. 18 (2016) 1355–1363.

[49] H.Z. Pengju Yang, Ruirui Wang Wei Lin, Xinchen Wang, Carbon vacancies in a melon polymeric matrix promote photocatalytic carbon dioxide conversion, Angew. Chem. 58 (2019) 1134–1137.

[50] H.X. Zhang, Q.L. Hong, J. Li, F. Wang, X. Huang, S. Chen, W. Tu, D. Yu, R. Xu, T. Zhou, J. Zhang, Isolated square-planar copper center in boron imidazolate nanocages for photocatalytic reduction of CO_2 to CO, Angew. Chem. 58 (2019) 11752–11756.

[51] J. Shan, F. Raziq, M. Humayun, W. Zhou, Y. Qu, G. Wang, Y. Li, Improved charge separation and surface activation via boron-doped layered polyhedron $SrTiO_3$ for co-catalyst free photocatalytic CO_2 conversion, Appl. Catal. B: Environ. 219 (2017) 10–17.

[52] D. Wang, R. Huang, W. Liu, D. Sun, Z. Li, Fe-based MOFs for photocatalytic CO_2 reduction: role of coordination unsaturated sites and dual excitation pathways, ACS Catal. 4 (2014) 4254–4260.

[53] H.X. Zhang, Q.L. Hong, J. Li, F. Wang, X. Huang, S. Chen, W. Tu, D. Yu, R. Xu, T. Zhou, J. Zhang, Isolated square-planar copper center in boron imidazolate nanocages for photocatalytic reduction of CO_2 to CO, Angew. Chem. 58 (2019) 11752–11756.

[54] Y.-H.Y. Chieh-Chao Yang, Bart van der Linden, Jeffrey C.S. Wu, Guido Mul, Artificial photosynthesis over crystalline TiO_2-based catalysts: fact or fiction? J. Am. Chem. Soc. 132 (2010) 8398–8406.

[55] L. Liu, C. Zhao, J.T. Miller, Y. Li, Mechanistic Study of CO_2 Photoreduction with H_2O on Cu/TiO_2 Nanocomposites by in Situ X-ray Absorption and Infrared Spectroscopies, J. Phys. Chem. C. 121 (2016) 490–499.

[56] T. Yan, N. Li, L. Wang, W. Ran, P.N. Duchesne, L. Wan, N.T. Nguyen, L. Wang, M. Xia, G.A. Ozin, Bismuth atom tailoring of indium oxide surface frustrated Lewis pairs boosts heterogeneous CO_2 photocatalytic hydrogenation, Nat. Commun. 11 (2020) 6095.

[57] P.L. Zhaoyu Ma, Liqun Ye, Ying Zhou, Fengyun Su, Chenghua Ding, Haiquan Xie, Yang Bai, Po Keung Wong,, Oxygen vacancies induced exciton dissociation of flexible BiOCl nanosheets for effective photocatalytic CO_2 conversion, J. Mater. Chem. A 5 (2017) 24995–25004.

[58] F. Tian, H. Zhang, S. Liu, T. Wu, J. Yu, D. Wang, X. Jin, C. Peng, Visible-light-driven CO_2 reduction to ethylene on CdS: enabled by structural relaxation-induced intermediate dimerization and enhanced by ZIF-8 coating, Appl. Catal. B: Environ. 285 (2021), 119834.

[59] F. Xu, B. Zhu, B. Cheng, J. Yu, J. Xu, 1D/2D TiO_2/MoS_2 hybrid nanostructures for enhanced photocatalytic CO_2 reduction, Adv. Opt. Mater. 6 (2018) 1800911.

[60] K.K. Bass, L. Estergreen, C.N. Savory, J. Buckeridge, D.O. Scanlon, P.I. Djurovich, S. E. Bradforth, M.E. Thompson, B.C. Melot, Vibronic structure in room temperature

photoluminescence of the halide perovskite $Cs_3Bi_2Br_9$, Inorg. Chem. 56 (2017) 42–45.